Electronic Supplementary Information

Dawson-type Polyoxometalates-based vacancies *g*-C_3N_4 composite-nanomaterials for efficient photocatalytic nitrogen fixation

Xiao-Hong Li,[a] Wei-Lin Chen,*[a] Peng He,[a] Ting Wang,[a] Ding Liu,[a] Yun-Wu Li,[b] Yang-Guang Li,*[a] and En-Bo Wang*[a]

[a]Key Laboratory of Polyoxometalate Science of Ministry of Education, Department of Chemistry, Northeast Normal University, Changchun 130024 (P. R. China).
Email: chenwl@nenu.edu.cn; liyg658@nenu.edu.cn; wangeb889@nenu.edu.cn;
[b]Shangdong Provincial Key Laboratory of Chemical Energy Storage and Novel Cell Technology, School of Chemistry and Chemical Engineering, Liaocheng University, Liaocheng 252059 (P. R. China).

Table of Contents

Supplementary Experimental Section

Photoelectrochemical measurements: The Time-resolved photocurrent curve was measured in a system of three-electrode on the CHI601D electrochemical workstation (Shanghai Chenhua Instrument Corp., China) with the Xenon lamp illuminate at room temperature. Composite-nanomaterials were dropping on the conductive glass FTO as the working electrode. A standard Ag/AgCl and Pt were served as reference electrode and counter electrode. The measurement was performed in electrolyte of Na_2SO_4 aqueous solution (0.1mol L^{-1}) at a speed of 0.1 A s^{-1} from 0 to 400 s both in N_2 and air conditions. Na_2SO_4 aqueous solution was imported into N_2 for 30 min moving away the air before testing and kept pouring into N_2 in the measurement process. The Cyclic voltammetry curves and electrochemical impedance measurement were carried out on a CHI601D electrochemical workstation (Shanghai Chenhua Instrument Corp., China) at room temperature by a three-electrode system. Glassy carbon electrode was the working electrode, a standard Ag/AgCl and Pt were reference electrode and counter electrode. The electrolyte was 0.05 mol L^{-1} KCl aqueous solution.

Material characterizations: Bruker AXS TENSOR-27 FTIR spectrometer by KBr pellets was used to test the IR spectra from 4000 cm^{-1} to 400 cm^{-1}. The datas of Powder X-ray diffraction (XRD) were acquired on a Bruker AXSD8 Advance diffractometer in a 2θ scope of 5-80° at a rate of 10° depending on Cu Ka radiation (λ = 1.5418 Å). Scanning electron microscope (SEM), Energy dispersive X-ray (EDX) and Energy dispersive spectroscopy (EDS) spectrometry Element mapping were completed by means of a FEI Quanta 200F microscope involving a 20 kV speeding up voltage. The Transmission electron microscope (TEM) images were performed with accelerating voltage of 200 kV on a JEOL-2100F transmission electron microscope. Nitrogen sorption isotherms were operated by ASAP 2020M micropore and mesopore analyzer. The XPS was completed on an ESCALAB 250Xi photoelectronic spectrometer of F-doped SnO_2 glass with an internal reference of C1s photoelectron at 284.6 eV peak and an Al Ka radiation X-ray source. The Uv-vis was tested at the spectral range from 200 nm to 900 nm on an Ultraviolet spectrophotometer of China SP-756P. The photoluminescent (PL) spectra was carried out on a Hitachi F-4500 fluorescence spectrophotometer.

Supplementary Physical and Chemical Characterizations

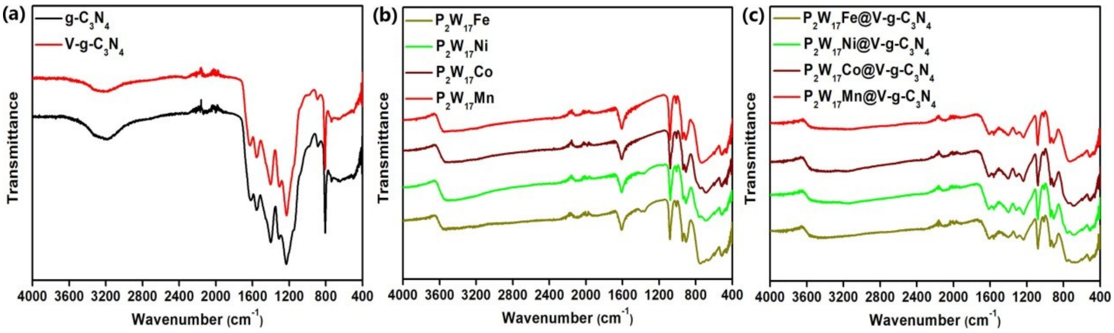

Figure S1. IR of (a) *g*-C_3N_4 and V-*g*-C_3N_4; (b) $P_2W_{17}Fe$, $P_2W_{17}Ni$, $P_2W_{17}Co$ and $P_2W_{17}Mn$; (c) $P_2W_{17}Fe$@V-*g*-C_3N_4, $P_2W_{17}Ni$@V-*g*-C_3N_4, $P_2W_{17}Co$@V-*g*-C_3N_4 and $P_2W_{17}Mn$@V-*g*-C_3N_4.

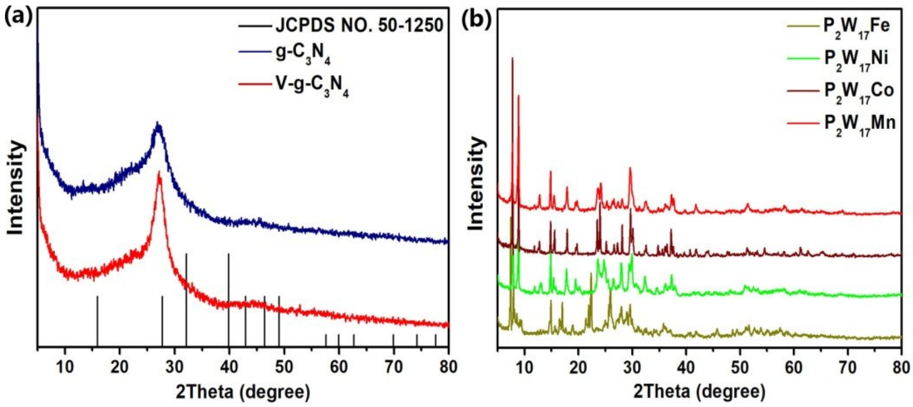

Figure S2. XRD of (a) simulated pwowder diffraction pattern of *g*-C_3N_4 and experimental measurement of *g*-C_3N_4 and V-*g*-C_3N_4; (b) $P_2W_{17}Fe$, $P_2W_{17}Ni$, $P_2W_{17}Co$ and $P_2W_{17}Mn$.

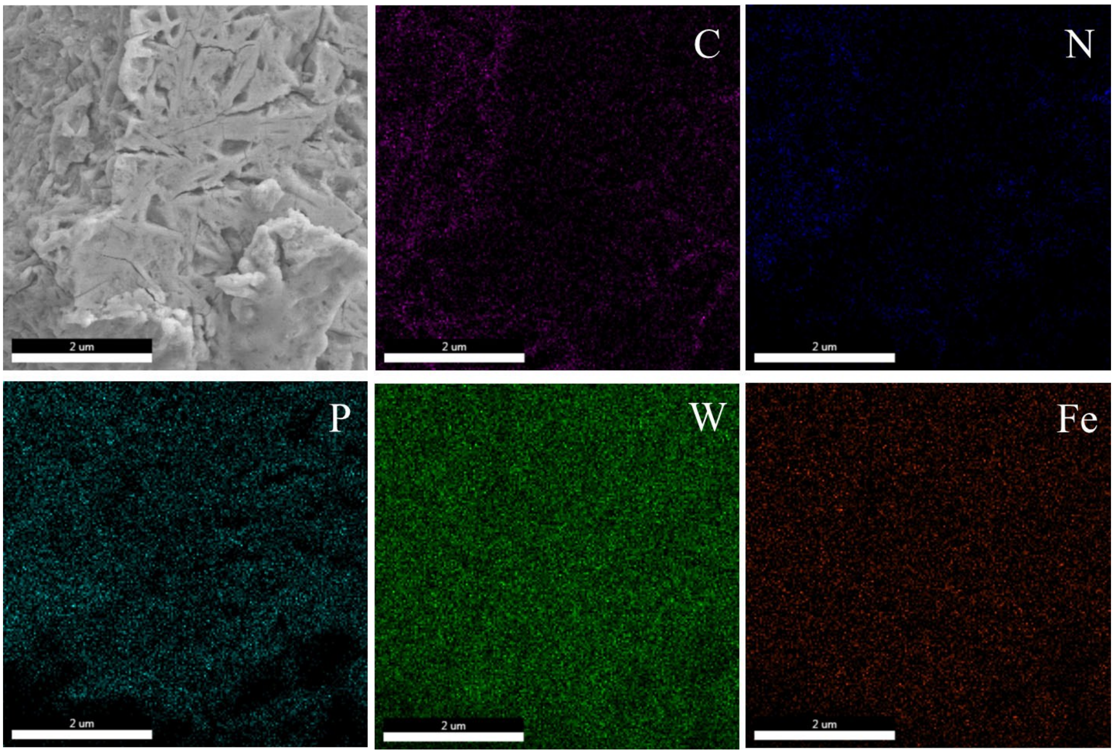

Figure S3. EDX Element mapping of $P_2W_{17}Fe@V\text{-}g\text{-}C_3N_4$.

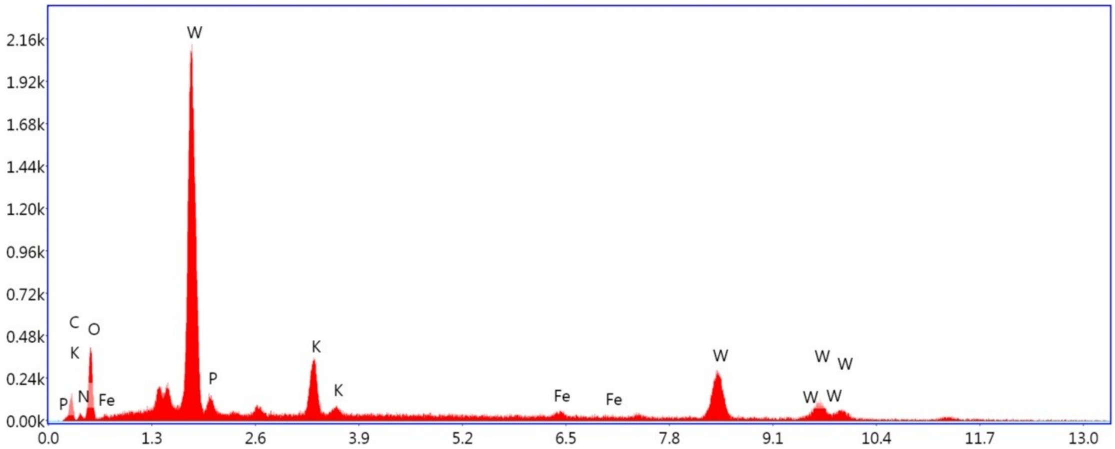

Figure S4. EDS of $P_2W_{17}Fe@V\text{-}g\text{-}C_3N_4$.

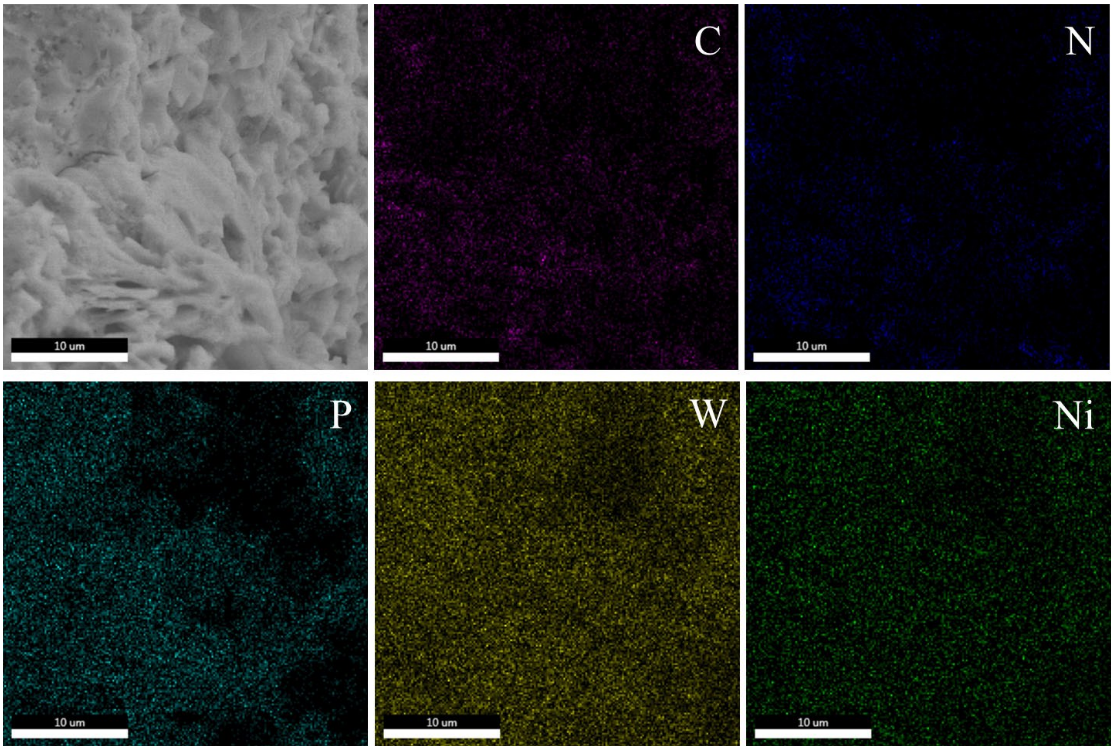

Figure S5. EDX Element mapping of $P_2W_{17}Ni@V$-*g*-C_3N_4.

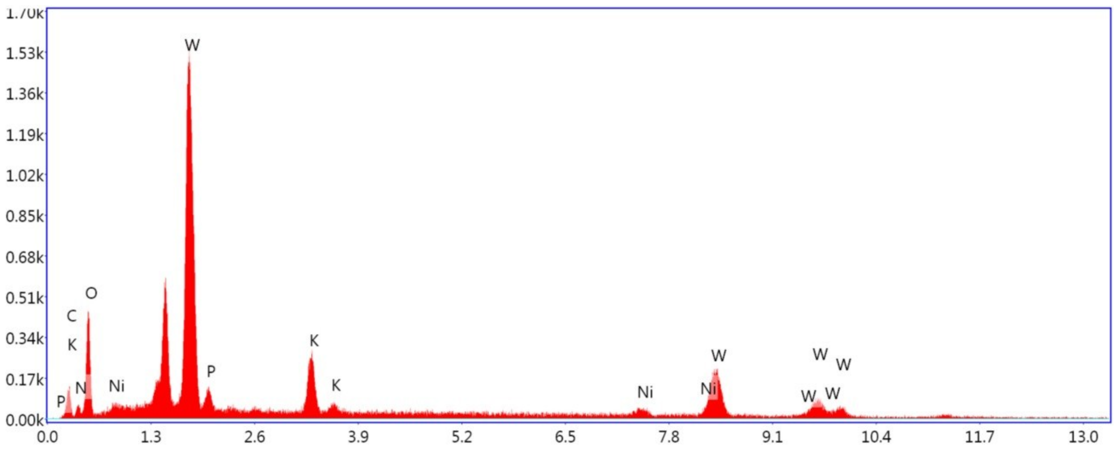

Figure S6. EDS of $P_2W_{17}Ni@V$-*g*-C_3N_4.

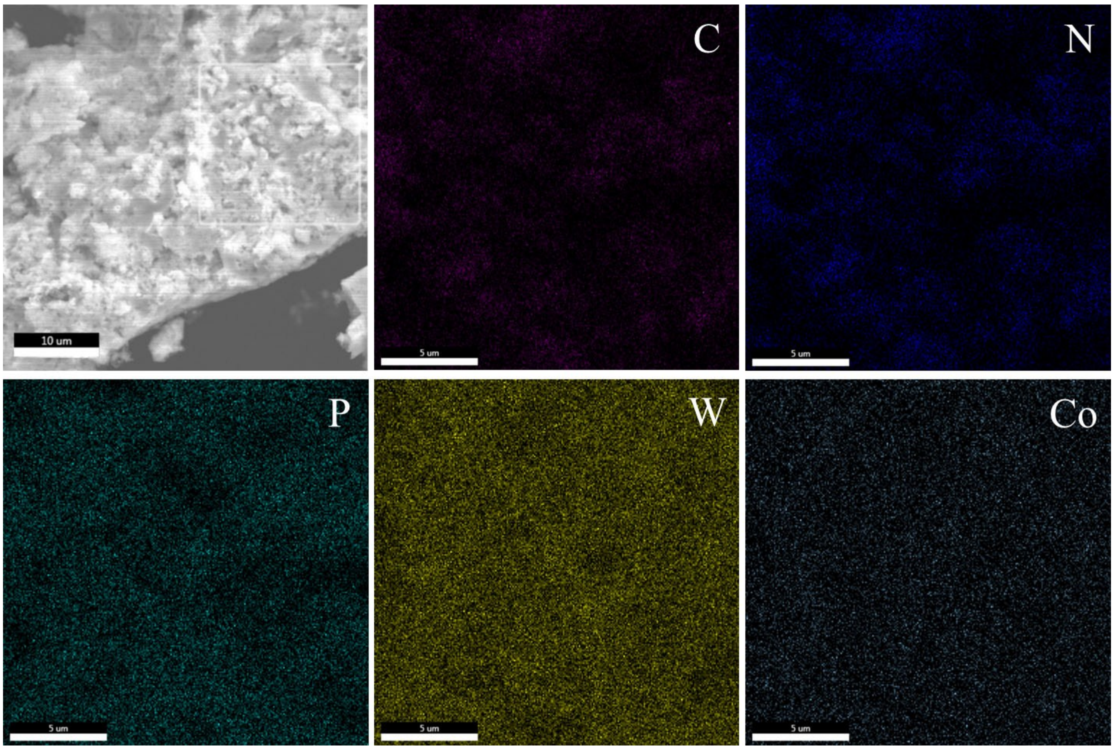

Figure S7. EDX Element mapping of $P_2W_{17}Co$@V-*g*-C_3N_4.

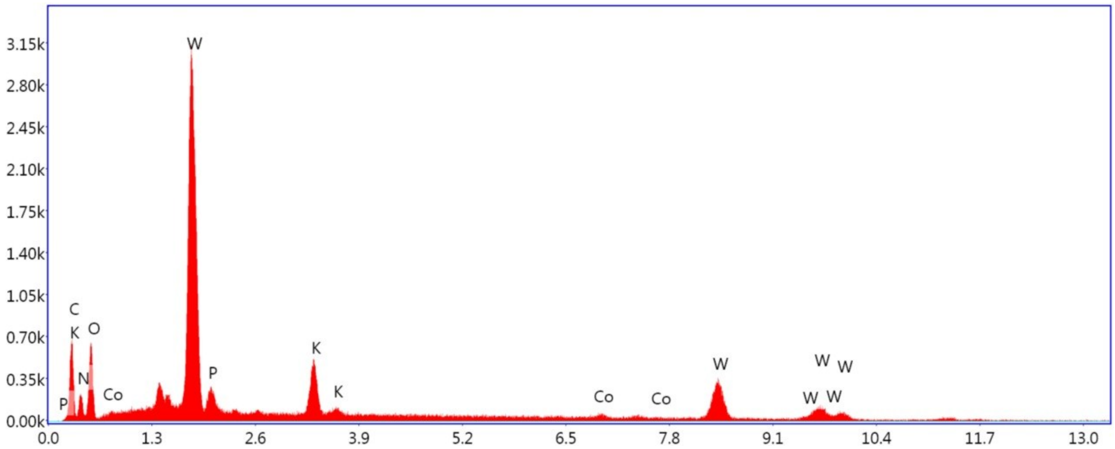

Figure S8. EDS of $P_2W_{17}Co$@V-*g*-C_3N_4.

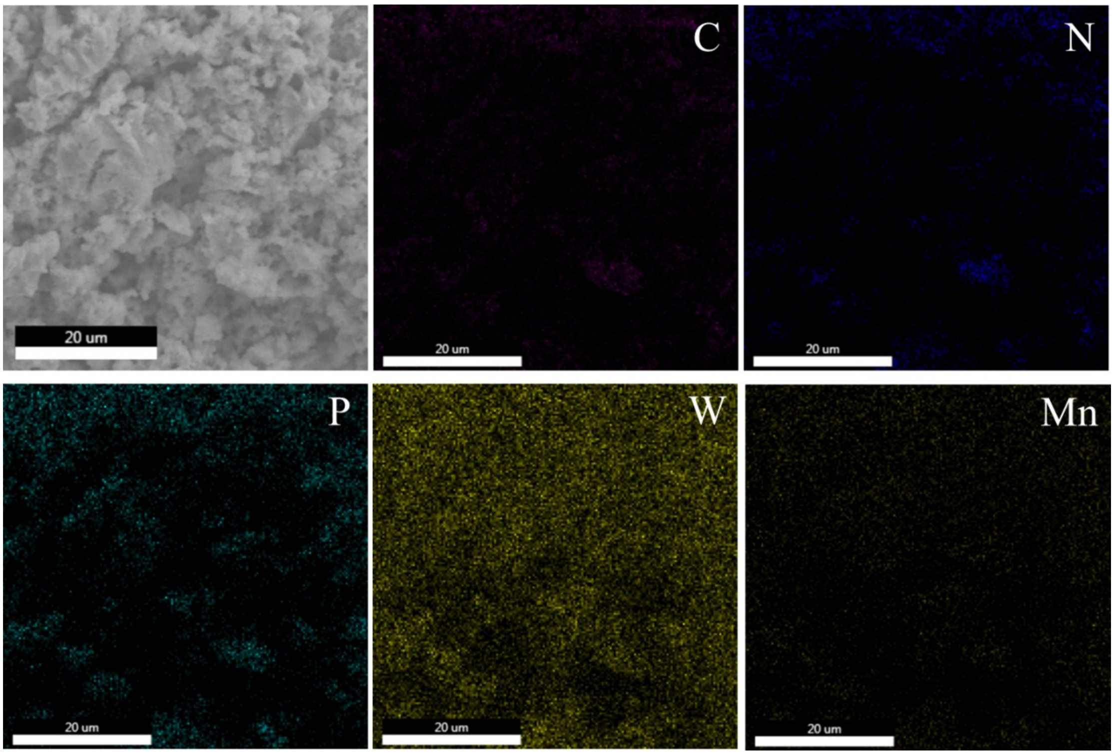

Figure S9. EDX Element mapping of $P_2W_{17}Mn$@V-*g*-C_3N_4.

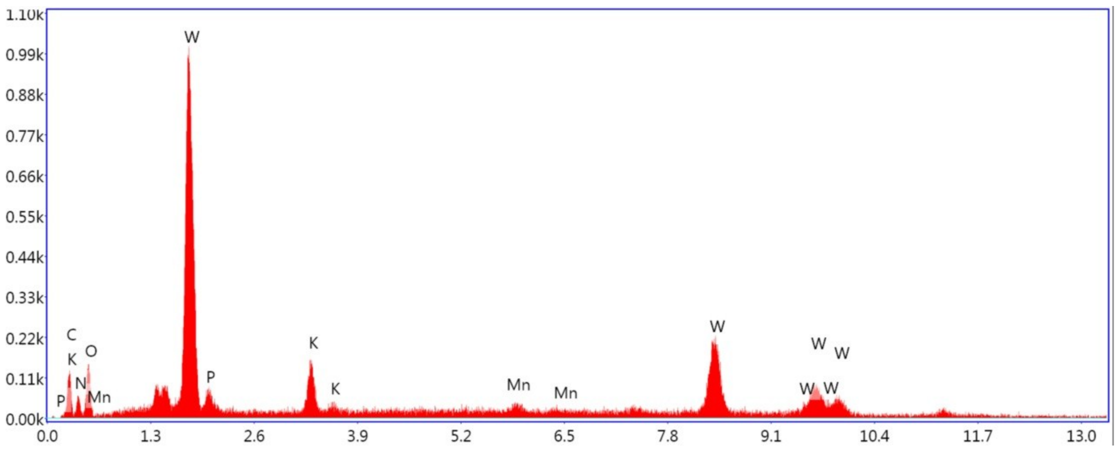

Figure S10. EDS of $P_2W_{17}Mn$@V-*g*-C_3N_4.

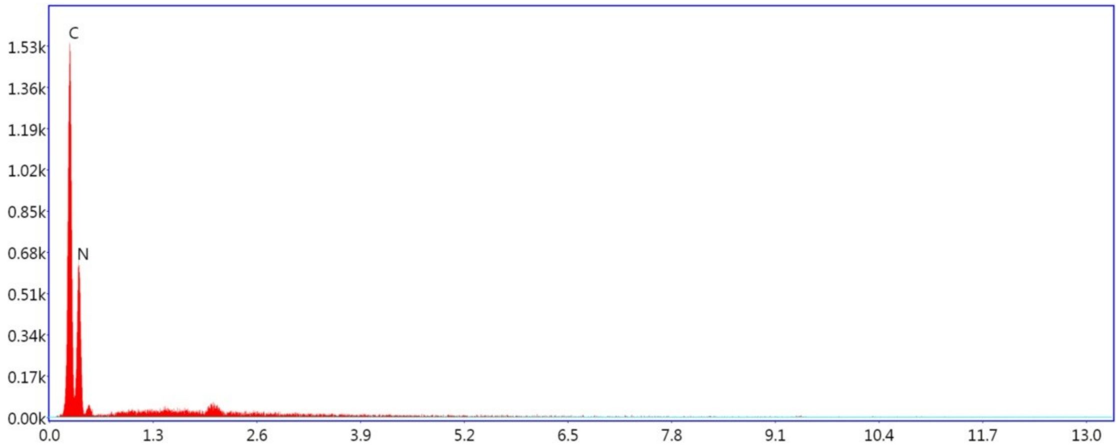

Figure S11. EDS of g-C_3N_4.

Table S1. The composition of elements for g-C_3N_4 obtained from EDS.

Element	*Weight/%*	*Atom/%*	*NET strength*
C	35.19	38.77	574.04
N	64.81	61.23	240.56

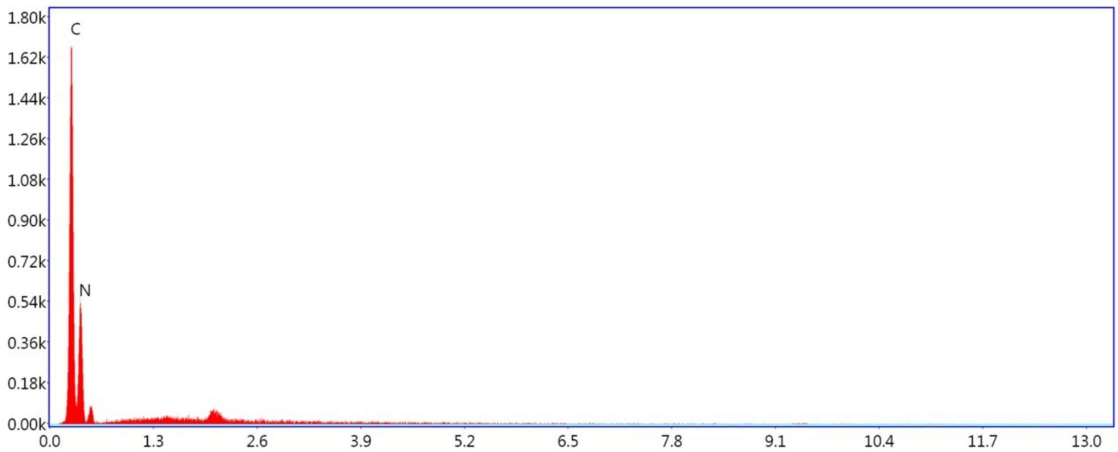

Figure S12. EDS of V-g-C_3N_4.

Table S2. The composition of elements for V-g-C_3N_4 obtained from EDS.

Element	*Weight/%*	*Atom/%*	*NET strength*
C	38.40	42.10	623.93
N	61.60	57.90	206.99

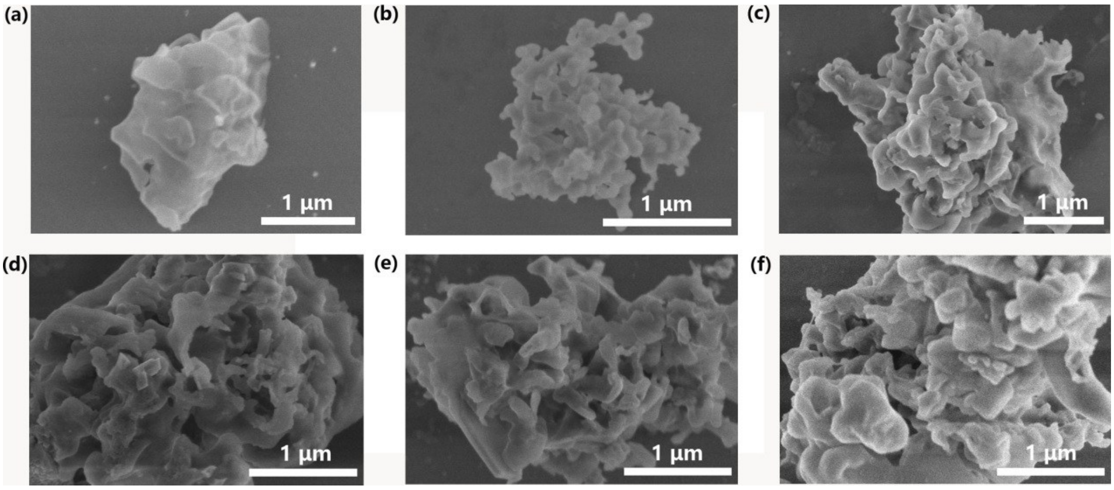

Figure S13. SEM images of (a) *g*-C_3N_4; (b) V-*g*-C_3N_4; (c) $P_2W_{17}Fe$@V-*g*-C_3N_4; (d) $P_2W_{17}Ni$@V-*g*-C_3N_4; (e) $P_2W_{17}Co$@V-*g*-C_3N_4; (f) $P_2W_{17}Mn$@V-*g*-C_3N_4.

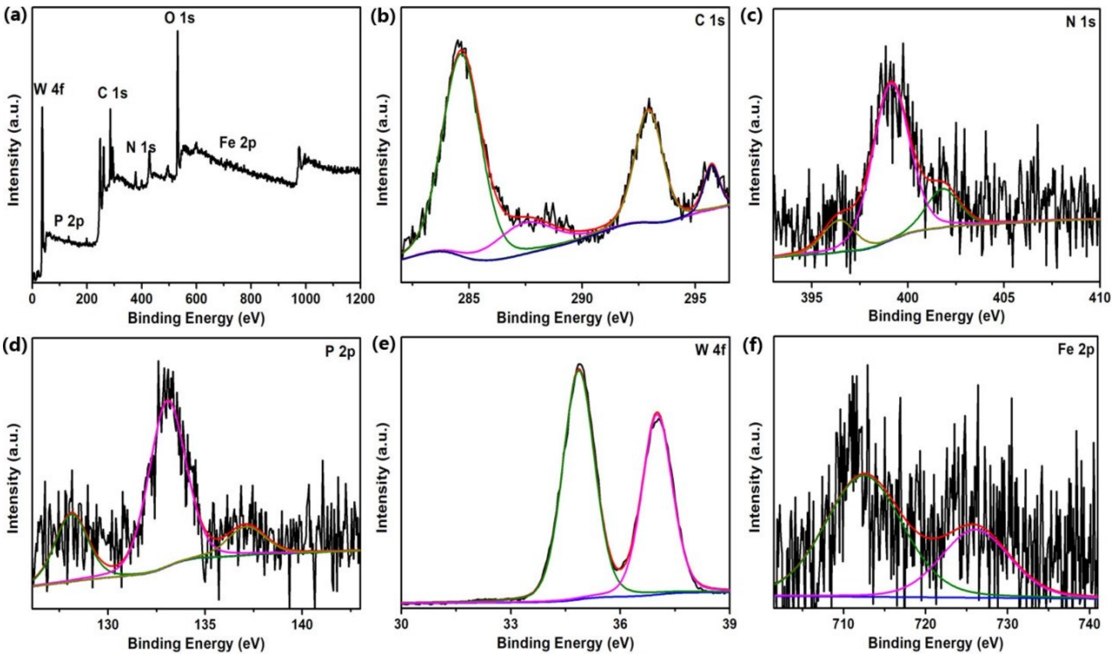

Figure S14. XPS of the $P_2W_{17}Fe@V\text{-}g\text{-}C_3N_4$; (b) the high resolution of the C 1s; (c) the high resolution of the N 1s; (d) the high resolution of the P 2p; (e) the high resolution of the W 4f; (f) the high resolution of the Fe 2p.

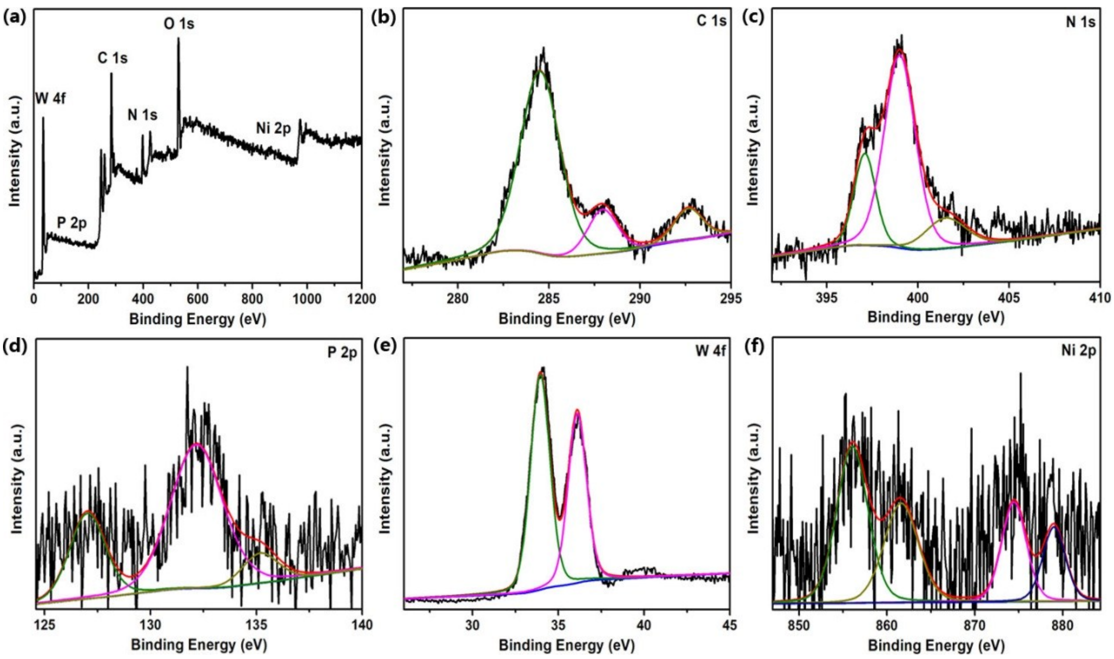

Figure S15. XPS of the $P_2W_{17}Ni@V\text{-}g\text{-}C_3N_4$; (b) the high resolution of the C 1s; (c) the high resolution of the N 1s; (d) the high resolution of the P 2p; (e) the high resolution of the W 4f; (f) the high resolution of the Ni 2p.

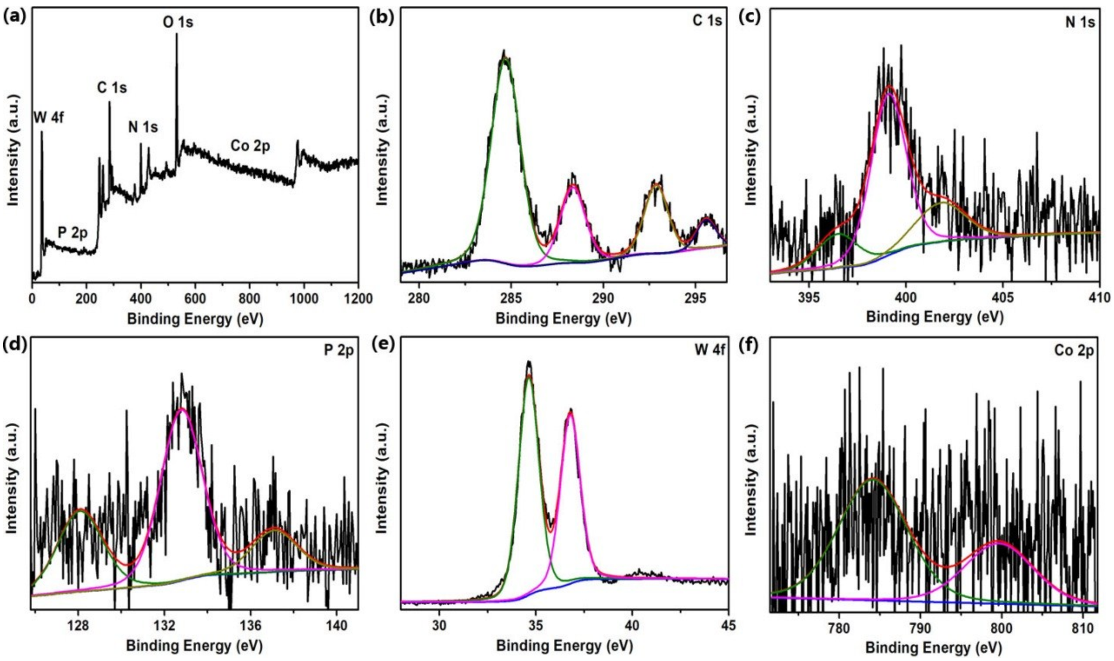

Figure S16. XPS of the $P_2W_{17}Co@V$-*g*-C_3N_4; (b) the high resolution of the C 1s; (c) the high resolution of the N 1s; (d) the high resolution of the P 2p; (e) the high resolution of the W 4f; (f) the high resolution of the Co 2p.

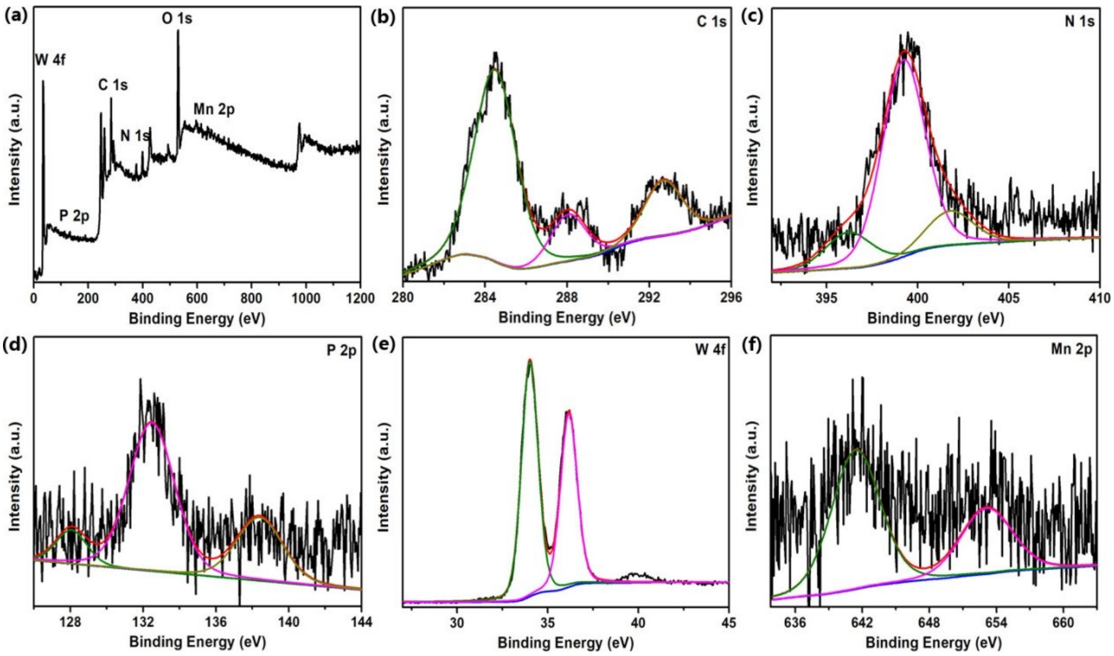

Figure S17. XPS of the $P_2W_{17}Mn@V$-*g*-C_3N_4; (b) the high resolution of the C 1s; (c) the high resolution of the N 1s; (d) the high resolution of the P 2p; (e) the high resolution of the W 4f; (f) the high resolution of the Mn 2p.

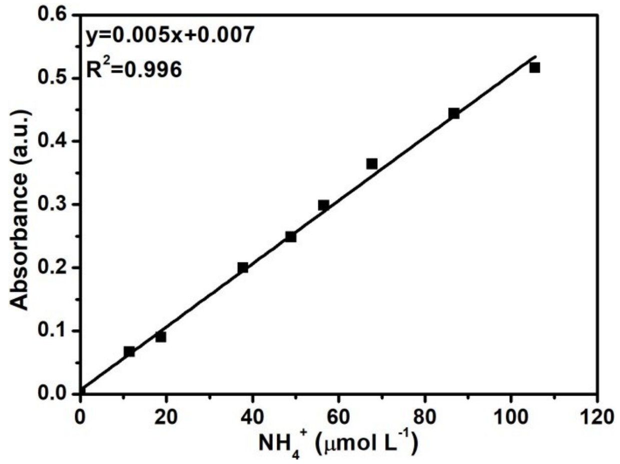

Figure S18. The standard curve line of NH_4^+ ions concentration detected by Nessler's reagent.

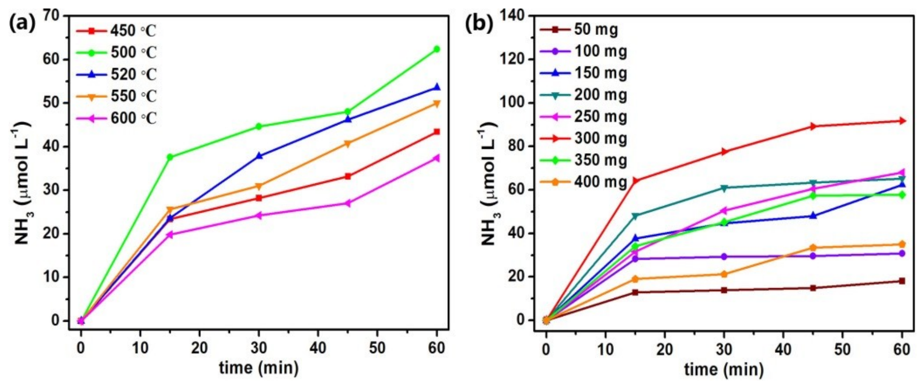

Figure S19. (a) NH_3 production at different temperature of V-*g*-C_3N_4 with $P_2W_{17}Fe$ composite nanomaterial; (b) NH_3 production at different amount of $P_2W_{17}Fe$ with 20 mg V-*g*-C_3N_4 composite nanomaterial.

Table S3. Comparison of photocatalytic N_2 fixation results with previously reported data.

catalyst	*NH_3 production rate*	*Light source*	*condition*	*ref.*
g-C_3N_4	3.01 mg L^{-1} h^{-1} g_{cat}^{-1}	250 W sodium lamp 400–800 nm	500 mL 0.789 g L^{-1} ethanol 0.2 g catalyst ambient pressure and 30 ℃	S1
g-C_3N_4	12.5 mg L^{-1} h^{-1} g_{cat}^{-1}	250 W high pressure sodium lamp 400-800 nm	500 mL 0.789 g L^{-1} ethanol, 0.2 g photocatalyst ambient pressure and 30 ℃	S2
g-C_3N_4	10.4 mg L^{-1} h^{-1} g^{-1}	250 W high pressure sodium lamp 400-800 nm	500 mL 0.789 g L^{-1} ethanol, 0.2 g photocatalyst ambient pressure and 30 ℃	S3
V-*g*-C_3N_4	1.24 mmol h^{-1} g^{-1}	300 W Xe lamp λ>420 nm	50 mL water of 20% methanol, 50 mg catalyst ambient temperature and atmospheric pressure	S4
V-*g*-C_3N_4	5.5 mg L^{-1} h^{-1} g_{cat}^{-1}	250 W high pressure sodium lamp 400-800 nm	500 mL water of 0.2 mL methanol or ethanol, 0.1 g catalyst	S5
g-C_3N_4/KOH	3.632 mmol h^{-1} g^{-1}	300 W Xe lamp	150 mL CH_3OH, 20 mg catalyst room temperature (25 ℃)	S6
g-C_3N_4/HCl	6.32 mg L^{-1} h^{-1} g_{cat}^{-1}	250 W sodium lamp 400-800 nm	500 mL of 0.789 g L^{-1} ethanol 0.2 g catalyst ambient pressure and 30 ℃	S7
Cu/*g*-C_3N_4	8.8 mg L^{-1} h^{-1} g_{cat}^{-1}	250 W sodium lamp 400-800 nm	500 mL water of 0.789 g L^{-1} ethanol, 0.2 g catalyst ambient pressure, temperature ~200 ℃	S8
S/*g*-C_3N_4	5.99 mM h^{-1} g_{cat}^{-1}	500 W Xe lamp	50 mL of 4 vol% methanol aqueous solution	S9
CdS/*g*-C_3N_4	3.18×10^3 µmol L^{-1} g^{-1}	500W Xe lamp	50 mL water of 0.789 g L^{-1} ethanol, 50 mg catalyst 25 ℃	S10
g-C_3N_4/rGO	9.276 mg L^{-1} h^{-1} g_{cat}^{-1}	250 W sodium lamp 400-800 nm	500 mL solution of 1 mmol L1EDTA-2Na 0.2 g catalyst ambient pressure and 30 ℃	S11
$PrCO_3OH$/*g*-C_3N_4	8.9 mM g^{-1} h^{-1}	500 W Xenon lamp	50 mL aqueous solution of 10 vol% methanol, 30 mg catalyst	S12
g-C_3N_4/Ag_2CO_3	11 mg L^{-1} h^{-1} g_{cat}^{-1}	250 W high pressure sodium lamp 400-800 nm	500 mL water of 0.2 mL methanol or ethanol, 0.1 g catalyst	S13
Fe_2O_3/*g*-C_3N_4	47.9 mg L^{-1} h^{-1}	300 W high pressure Xenon lamp	100 mL of 20% ethanol solution 40 mg photocatalyst room temperature and atmospheric pressure	S14
Fe_2O_3/*g*-C_3N_4	4380 µmol L^{-1} h^{-1}	300 W Xe lamp	100 mL distilled water, 0.1 g catalyst room temperature of 25 ℃	S15
$W_{18}O_{49}$/*g*-C_3N_4	2.6 mg L^{-1} h^{-1} g_{cat}^{-1}	300 W Xe lamp and 200 W infrared light	500 mL 0.789 g L^{-1} ethanol, 0.2 g photocatalyst	S16
Ag/*g*-C_3N_4/$W_{18}O_{49}$	0.57 mg L^{-1} h^{-1} g_{cat}^{-1}	300 W Xe lamp and 200 W infrared light	500 mL 0.789 g L^{-1} ethanol, 0.2 g photocatalyst	S17
Ga_2O_3-DBD/*g*-C_3N_4	112.5 µmol L^{-1} h^{-1}	500 W Xe lamp	50 mL water of 0.04 mmol methanol, 0.02 g catalyst	S18

g-$C_3N_4/Zn_{0.11}Sn_{0.12}Cd_{0.88}S_{1.12}$	7.543 mg L^{-1} h^{-1} g_{cat}^{-1}	250 W sodium lamp 400-800 nm	500 mL water of 0.789 g L^{-1} ethanol, 0.2 g catalyst ambient pressure and 30 ℃	S19
g-C_3N_4/ZnMoCdS	1.47 mg L^{-1} h^{-1} g_{cat}^{-1}	250 W sodium lamp 400-800 nm	500 mL water of 0.789 g L^{-1} ethanol, 0.2 g catalyst ambient pressure and 30 ℃	S20
g-$C_3N_4/Mg_{1.1}Al_{0.3}Fe_{0.2}O_{1.7}$	7.5 mg L^{-1} h^{-1} g_{cat}^{-1}	250 W sodium lamp 400-800 nm	500 mL water of 0.789 g L^{-1} ethanol, 0.2 g catalyst ambient pressure and 30 ℃	S21
P_2W_{17}Fe@V-*g*-C_3N_4	91.8 μmol L^{-1} h^{-1}	300 W Xenon lamp	80 mL water and 20 ml ethanol, 300 mg catalyst atmospheric pressure and room temperature	our work
P_2W_{17}Ni@V-*g*-C_3N_4	208 μmol L^{-1} h^{-1}	300 W Xenon lamp	80 mL water and 20 ml ethanol, 300 mg catalyst atmospheric pressure and room temperature	our work
P_2W_{17}Co@V-*g*-C_3N_4	214.6 μmol L^{-1} h^{-1}	300 W Xenon lamp	80 mL water and 20 ml ethanol, 300 mg catalyst atmospheric pressure and room temperature	our work
P_2W_{17}Mn@V-*g*-C_3N_4	99.2 μmol L^{-1} h^{-1}	300 W Xenon lamp	80 mL water and 20 ml ethanol, 300 mg catalyst atmospheric pressure and room temperature	our work

Table S4. Comparison of TON, TOF and STA efficiency for photocatalytic N_2 fixation with previously reported data.

catalyst	*NH_3 production rate*	*TON*	*TOF*	*STA*	*ref.*
TiO_2	0.73 µmol h-1	1.05		0.02%	S22
$W_{18}O_{49}$	195.5 µmol $h^{-1}\cdot g_{cat}^{-1}$			0.028%	S23
Bi_5O_7I	111.5 µmol $L^{-1}\cdot h^{-1}$		49.23 h^{-1}		S24
β-Ga_2O_3	0.0493 µmol $L^{-1}\cdot s^{-1}$		0.493 µmol $g^{-1}\cdot s^{-1}$		S25
$Au/(BiO)_2CO_3$	38.23 µg $h^{-1}\cdot mg_{cat}^{-1}$			0.006%	S26
Fe@3DGraphene	408±68 µg $h^{-1}\cdot g_{cat}^{-1}$		78		S27
FeMoS inorganic clusters	0.17 µmol $L^{-1}\cdot h^{-1}$	8 µmol μM^{-1}			S28
$[Mo_2Fe_6S_8(SPh)_3$	0.7 µmol $L^{-1}\cdot h^{-1}$	17			S29
$P_2W_{17}Fe@V$-*g*-C_3N_4	91.8 µmol L^{-1} h^{-1}	142 mmol M^{-1}	142 mmol M^{-1} h^{-1}	0.020%	our work
$P_2W_{17}Ni@V$-*g*-C_3N_4	208 µmol L^{-1} h^{-1}	338 mmol M^{-1}	338 mmol M^{-1} h^{-1}	0.045%	our work
$P_2W_{17}Co@V$-*g*-C_3N_4	214.6 µmol L^{-1} h^{-1}	346 mmol M^{-1}	346 mmol M^{-1} h^{-1}	0.046%	our work
$P_2W_{17}Mn@V$-*g*-C_3N_4	99.2 µmol L^{-1} h^{-1}	156 mmol M^{-1}	156 mmol M^{-1}	0.021%	our work

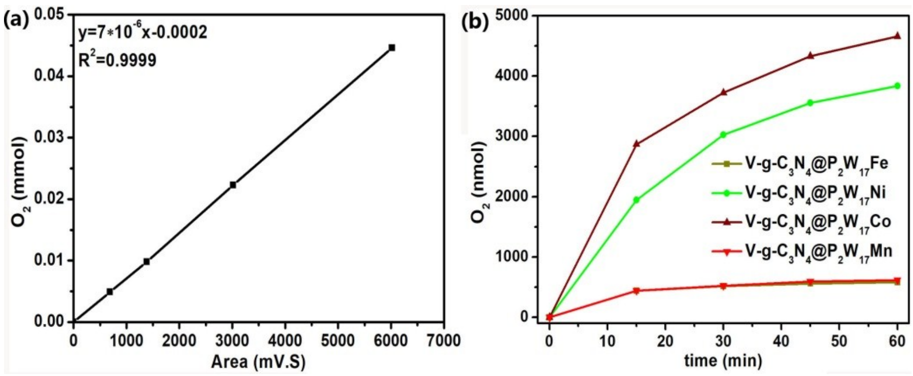

Figure S20. (a) the standard curve line of O_2 concentration; (b) O_2 production at different times of $P_2W_{17}Fe@V$-*g*-C_3N_4, $P_2W_{17}Ni@V$-*g*-C_3N_4, $P_2W_{17}Co@V$-*g*-C_3N_4 and $P_2W_{17}Mn@V$-*g*-C_3N_4.

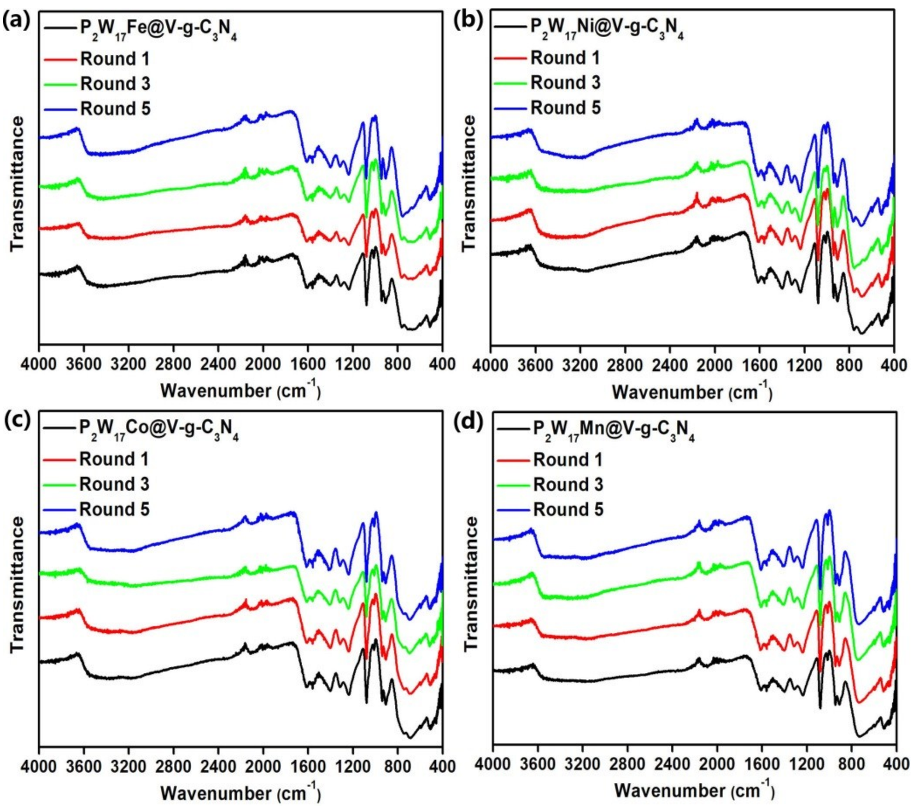

Figure S21. FTIR spectra of (a) $P_2W_{17}Fe@V$-*g*-C_3N_4 before and after each reaction; (b) $P_2W_{17}Ni@V$-*g*-C_3N_4 before and after each reaction; (c) $P_2W_{17}Co@V$-*g*-C_3N_4 before and after each reaction; (d) $P_2W_{17}Mn@V$-*g*-C_3N_4 before and after each reaction.

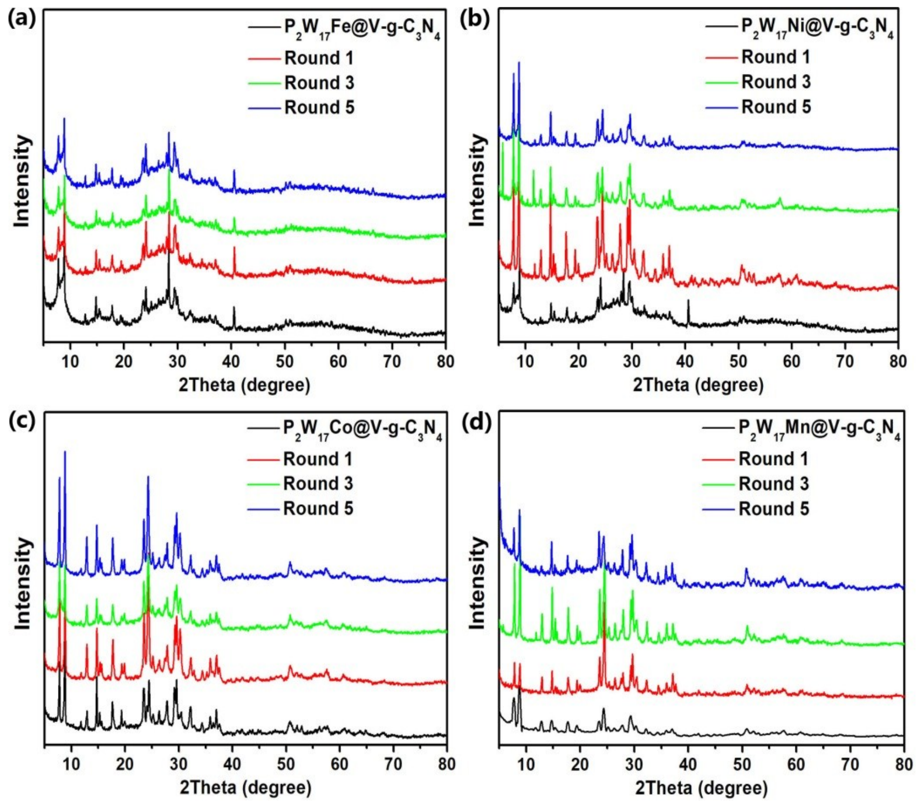

Figure S22. XRD of (a) $P_2W_{17}Fe@V$-*g*-C_3N_4 before and after each reaction; (b) $P_2W_{17}Ni@V$-*g*-C_3N_4 before and after each reaction; (c) $P_2W_{17}Co@V$-*g*-C_3N_4 before and after each reaction; (d) $P_2W_{17}Mn@V$-*g*-C_3N_4 before and after each reaction.

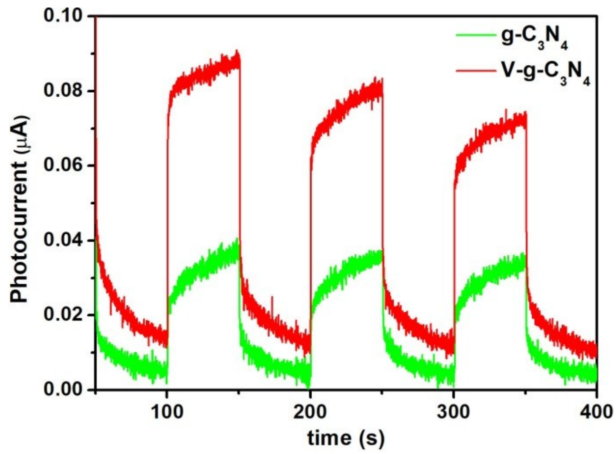

Figure S23. The time-resolved photocurrent curve of *g*-C_3N_4 and V-*g*-C_3N_4 in air atmosphere.

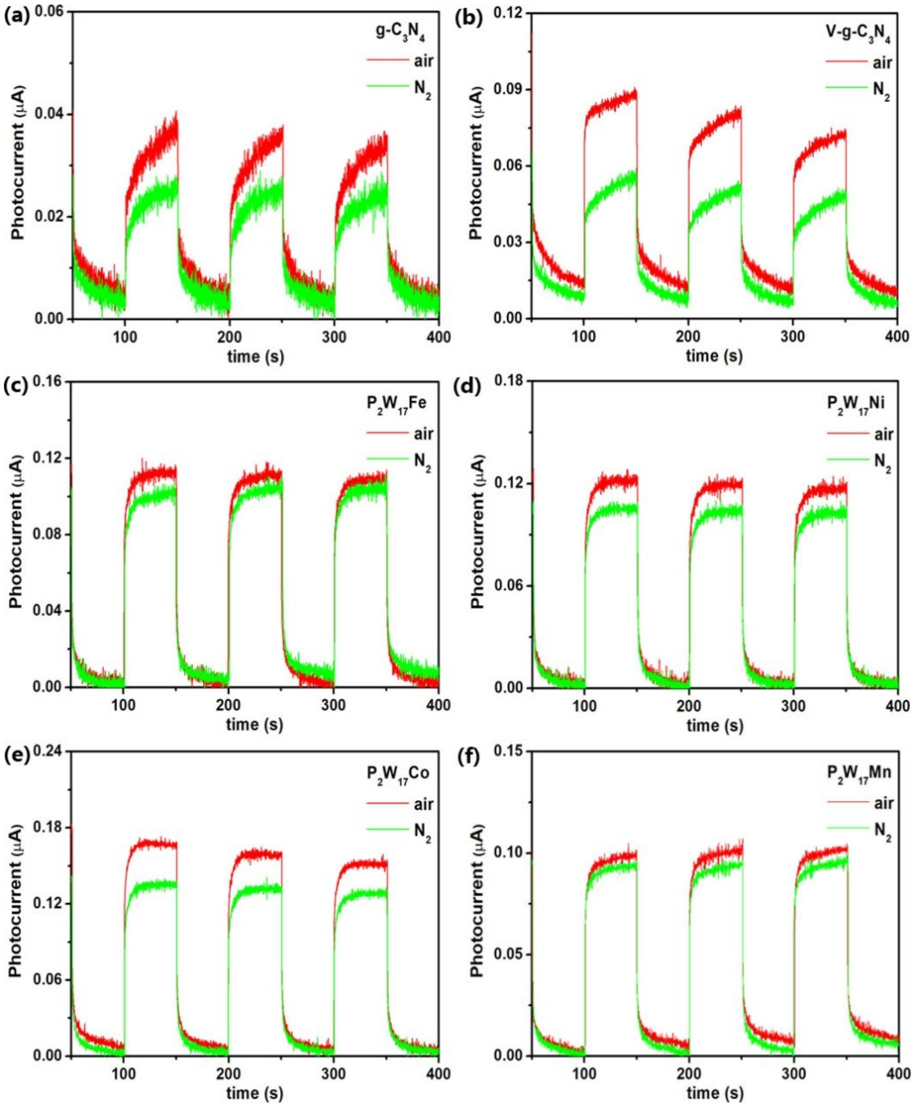

Figure S24. Comparison of the time-resolved photocurrent curve of (a) *g*-C_3N_4; (b) V-*g*-C_3N_4; (c) $P_2W_{17}Fe$; (d) $P_2W_{17}Ni$; (e) $P_2W_{17}Co$; (f) $P_2W_{17}Mn$ in air and N_2 atmosphere.

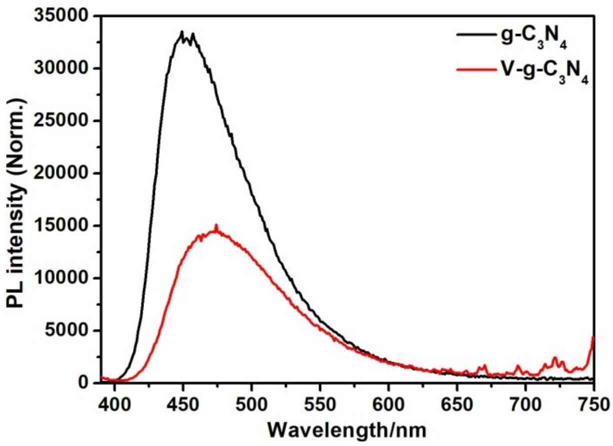

Figure S25. PL spectra of *g*-C_3N_4 and V-*g*-C_3N_4.

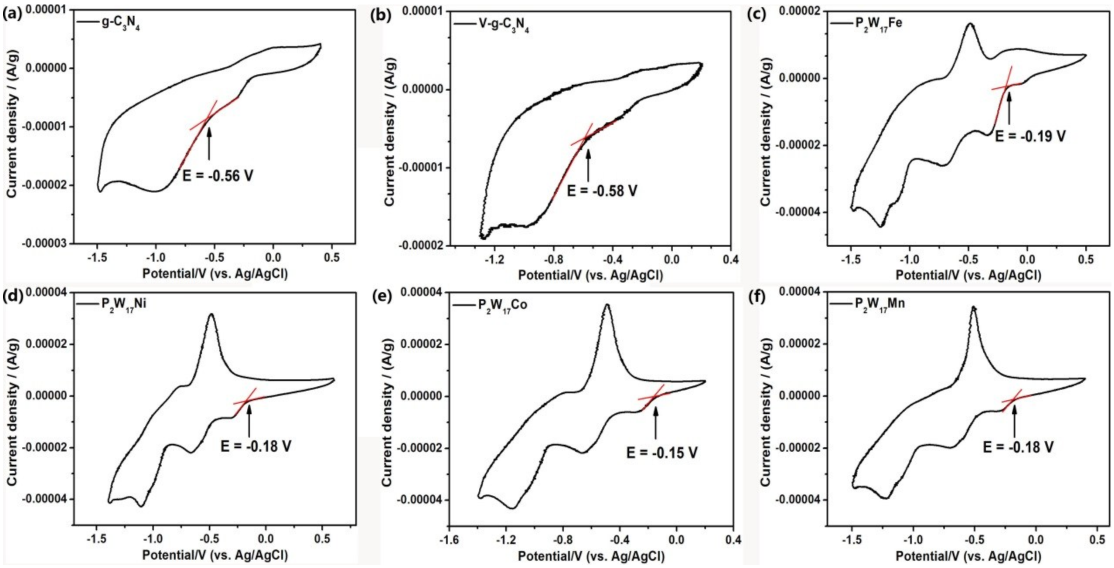

Figure S26. CV curves for (a) *g*-C_3N_4; (b) V-*g*-C_3N_4; (c) $P_2W_{17}Fe$@V-*g*-C_3N_4; (d) $P_2W_{17}Ni$@V-*g*-C_3N_4; (e) $P_2W_{17}Co$@V-*g*-C_3N_4; (f) $P_2W_{17}Mn$@V-*g*-C_3N_4.

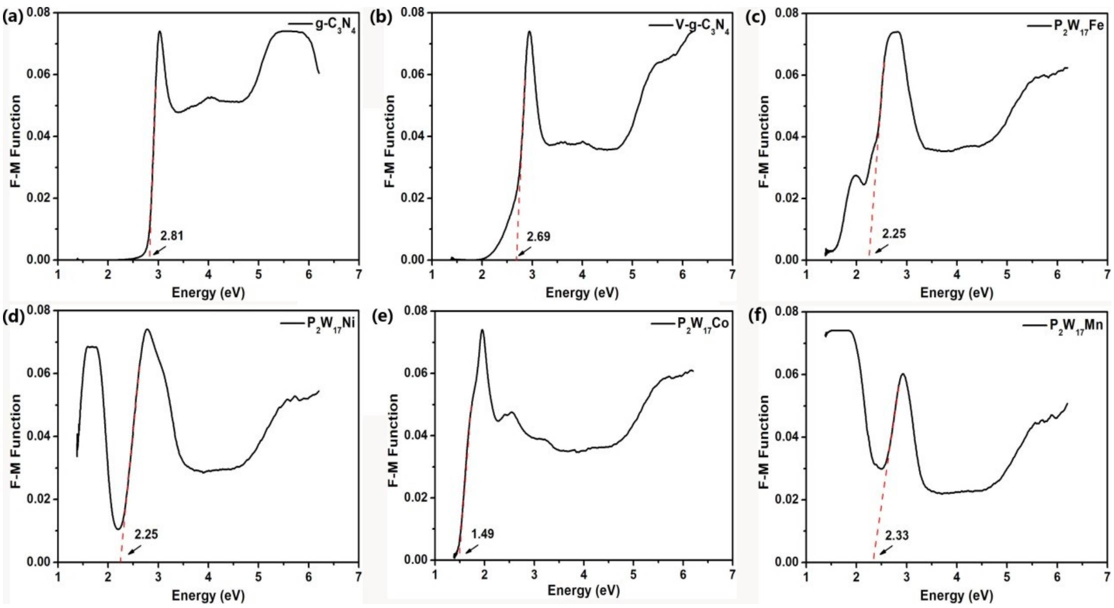

Figure S27. The plot of F against energy E for (a) *g*-C_3N_4; (b) V-*g*-C_3N_4; (c) $P_2W_{17}Fe$@V-*g*-C_3N_4; (d) $P_2W_{17}Ni$@V-*g*-C_3N_4; (e) $P_2W_{17}Co$@V-*g*-C_3N_4; (f) $P_2W_{17}Mn$@V-*g*-C_3N_4. The red line is the tangent of the curve and the intersection value is the band gap.

Table S5. The composition of elements for $P_2W_{17}Fe@V$-*g*-C_3N_4 obtained from EDS.

Element	*Weight/%*	*Atom/%*	*NET strength*
C	12.06	32.87	55.92
N	4.07	9.51	11.91
P	1.03	1.09	27.65
O	19.93	40.75	158.35
K	5.98	5.00	222.01
W	55.35	9.85	291.01
Fe	1.58	0.93	34.73

Table S6. The composition of elements for $P_2W_{17}Ni@V$-*g*-C_3N_4 obtained from EDS.

Element	*Weight/%*	*Atom/%*	*NET strength*
C	11.86	27.84	49.83
N	7.55	15.19	20.72
P	1.30	1.18	33.07
O	24.93	43.93	173.32
K	5.07	3.65	171.24
W	47.31	7.25	212.90
Ni	1.98	0.95	30.44

Table S7. The composition of elements for $P_2W_{17}Co@V$-*g*-C_3N_4 obtained from EDS.

Element	*Weight/%*	*Atom/%*	*NET strength*
C	22.80	41.31	251.32
N	15.65	24.32	83.64
P	1.10	0.78	73.12
O	19.81	26.95	245.17
K	3.70	2.06	299.03
W	36.05	4.27	352.32
Co	0.88	0.33	32.15

Table S8. The composition of elements for $P_2W_{17}Mn@V$-*g*-C_3N_4 obtained from EDS.

Element	*Weight/%*	*Atom/%*	*NET strength*
C	13.89	38.64	46.85
N	9.74	23.22	21.61
P	1.14	1.22	21.69
O	10.69	22.31	56.00
K	3.24	2.77	86.99
W	59.66	10.84	234.14
Mn	1.64	1.00	29.34

Notes and references

1 H. Q. Ma, Z. Y. Shi, S. Li and N. Liu, Large-scale production of graphitic carbon nitride with outstanding nitrogen photofixation ability via a convenient microwave treatment. *Appl. Surf. Sci.*, 2016, **379**, 309-315. DOI: org/10.1016/j.apsusc.2016.04.085.

2 S. J. Li, X. Chen, S. Z. Hu, Q. Li, J. Bai and F. Wang, Infrared ray assisted microwave synthesis: a convenient method for large-scale production of graphitic carbon nitride with outstanding nitrogen photofixation ability, *RSC Adv.*, 2016, **6**, 45931-45937. DOI: 10.1039/c6ra08817a.

3 J. Bai, X. Chen, Z. Y. Xi, X. Wang, Q. Li, and S. Z. Hu, Effect of solvothermal post-treatment on ammonia production performance of graphite phase carbonitride. *Acta Phys. Chim. Sin.*, 2017, **33**, 611-619. DOI: 10.3866/PKU.WHXB201611102.

4 G. H. Dong, W. K. Ho and C. Y. Wang, Selective photocatalytic N_2 fixation dependent on *g*-C_3N_4 induced by nitrogen vacancies. *J. Mater. Chem. A*, 2015, **3**, 23435-23441. DOI: 10.1039/c5ta06540b.

5 Y. F. Zhao, E. D. Wang and R. R. Jin, The effect of oxygen on the N_2 photofixation ability over N vacancies embedded *g*-C_3N_4 prepared by dielectric barrier discharge plasma treatment. *Diamond Relat. Mater.*, 2019, **94**, 146-154. DOI: org/10.1016/j.diamond.2019.03.004.

6 X. M. Li, X. Sun, L. Zhang, S. M. Sun and W. Z. Wang, Efficient photocatalytic fixation of N_2 by KOH-treated *g*-C_3N_4. *J. Mater. Chem. A*, 2018, **6**, 3005-3011. DOI: 10.1039/c7ta09762j.

7 H. Q. Ma, Z. Y. Shi, Q. Li and S. Li, Preparation of graphitic carbon nitride with large specific surface area and outstanding N_2 photofixation ability via a dissolve-regrowth process. *J. Phys. Chem. Solids*, 2016, **99**, 51-58. Doi: org/10.1016/j.jpcs.2016.08.008.

8 S. Z. Hu, X. Y. Qu, J. Bai, P. Li, Q. Li, F. Wang and L. J. Song, Effect of Cu(I)-N Active Sites on the N_2 Photofixation Ability over Flowerlike Copper-Doped *g*-C_3N_4 Prepared via a Novel Molten Salt-Assisted Microwave Process: The Experimental and Density Functional Theory Simulation Analysis. *ACS Sustainable Chem. Eng.*, 2017, **5**, 6863-6872. DOI: 10.1021/acssuschemeng.7b01089.

9 S. H. Cao, B. Fan, Y. C. Feng, H. Chen, F. Jiang and X. Wang, Sulfur-doped *g*-C_3N_4 nanosheets with carbon vacancies: General synthesis and improved activity for simulated solar-light photocatalytic nitrogen fixation. *Chem. Eng. J.*, 2018, **353**, 147-156. DOI: org/10.1016/j.cej.2018.07.116.

10 H. D. Khalilabad, A. H. Yangjeh, D. Seifzadeh, S. A. Khaneghah and E. V. Kermani, *g*-C_3N_4 nanosheets decorated with carbon dots and CdS nanoparticles: Novel nanocomposites with excellent nitrogen photofxation ability under simulated solar irradiation. *Ceram. Int.*, 2019, **45**, 2542-2555. DOI: org/10.1016/j.ceramint.2018.10.185.

11 S. Z. Hu, W. D. Zhang, J. Bai, G. Lu, L. Zhang and G. Wu, Construction of a 2D/2D *g*-C_3N_4/rGO hybrid heterojunction catalyst with outstanding charge separation ability and nitrogen photofixation performance via a surface protonation process. *RSC Adv.*, 2016, **6**, 25695-25702. DOI: 10.1039/c5ra28123g.

12 X. W. Feng, H. Chen, F. Jiang and X. Wang, In-situ self-sacrificial fabrication of lanthanide hydroxycarbonates/graphitic carbon nitride heterojunctions: nitrogen photofixation under simulated solar light irradiation. *Chem. Eng. J.*, 2018, **347**, 849-859. DOI: org/10.1016/j.cej.2018.04.157.

13 G. Wu, L. H. Yu, Y. F. Liu, J. M. Zhao, Z. Han and G. Geng, One step synthesis of N vacancy-doped *g*-C_3N_4/Ag_2CO_3 heterojunction catalyst with outstanding "two-path" photocatalytic N_2 fixation ability via in-situ self-sacrificial method. *Appl. Surf. Sci.*, 2019, **481**, 649-660. DOI: org/10.1016/j.apsusc.2019.03.112.

14 S. Z. Liu, S B. Wang, Y. Jiang, Z. Q. Zhao, G. Y. Jiang and Z. Y. Synthesis of Fe_2O_3 loaded porous *g*-C_3N_4 photocatalyst for photocatalytic reduction of dinitrogen to ammonia. *Chem. Eng. J.*, 2019, **373**, 572-579. DOI: org/10.1016/j.cej.2019.05.021.

15 H. Y. Mou, J. F. Wang, D. L. Zhang, D. K. Yu, W. J. Chen, D. B. Wang and T. C. Mu, A one-step deep eutectic solvent assisted synthesis of carbon nitride/metal oxide composites for photocatalytic nitrogen fixation. *J. Mater. Chem. A*, 2019, **7**, 5719-5725. DOI: 10.1039/c8ta11681d.

16 H. Y. Liang, H. Zou and S. Z. Hu, Preparation of the $W_{18}O_{49}$/*g*-C_3N_4 heterojunction catalyst with full-spectrum-driven photocatalytic N_2 photofixation ability from the UV to near infrared region. *New J. Chem.,* 2017, **41**, 8920-8926. DOI: 10.1039/c7nj01848g.

17 H. Y. Liang, J. Z. Li and Y. W. Tian, Construction of full-spectrum-driven Ag–*g*-C_3N_4/$W_{18}O_{49}$ heterojunction catalyst with outstanding N_2 photofixation ability. *RSC Adv.*, 2017, **7**, 42997-43004. DOI: 10.1039/c7ra08420j.

18 S. H. Cao, N. Zhou, F. H. Gao, H. Chen and F. Jiang, All-solid-state Z-scheme 3,4-dihydroxybenzaldehyde-functionalized Ga_2O_3/graphitic carbon nitride photocatalyst with aromatic rings as electron mediators for visible-light photocatalytic nitrogen fixation. *Appl. Catal., B*, 2017, **218**, 600-610. DOI: org/10.1016/j.apcatb.2017.07.013.

19 S. Z. Hu, Y. M. Li, F. Y. Li, Z. P. Fan, H. F. Ma, W. Li and X. X. Kang, Construction of *g*-C_3N_4/$Zn_{0.11}Sn_{0.12}Cd_{0.88}S_{1.12}$ Hybrid Heterojunction Catalyst with Outstanding Nitrogen Photofixation Performance Induced by Sulfur Vacancies. *ACS Sustainable Chem. Eng.*, 2016, **4**, 2269-2278. DOI: 10.1021/acssuschemeng.5b01742.

20 Q. Zhang, S. Z. Hu, Z. P. Fan, D. S. Liu, Y. F. Zhao, H. F. Ma and F. Y. Li, Preparation of *g*-C_3N_4/ZnMoCdS hybrid heterojunction catalyst with outstanding nitrogen photofixation performance under visible light via hydrothermal post-treatment. *Dalton Trans.*, 2016, **45**, 3497-3505. DOI: 10.1039/c5dt04901f.

21 Y. J. Wang, W. S. Wei, M. Y. Li, S. Z. Hu, J. Zhang and R. J. Feng, In situ construction of Z-scheme *g*-C_3N_4/$Mg_{1.1}Al_{0.3}Fe_{0.2}O_{1.7}$ nanorod heterostructures with high N_2 photofixation ability under visible light. *RSC Adv.*, 2017, **7**, 18099-18107. DOI: 10.1039/c7ra00097a.

22 H. Hirakawa, M. Hashimoto, Y. Shiraishi and T. Hirai, Photocatalytic Conversion of Nitrogen to Ammonia with Water on Surface Oxygen Vacancies of Titanium Dioxide. *J. Am. Chem. Soc.*, 2017, **139**, 10929-10936. DOI: 10.1021/jacs.7b06634.

23 N. Zhang, A. Jalil, D. X. Wu, S. M. Chen, Y. F. Liu, C. Gao, W. Ye, Z. M. Qi, H. X. Ju, C. M. Wang, X. J. Wu, L. Song, J. F. Zhu and Y. J. Xiong, Refining Defect States in $W_{18}O_{49}$ by Mo Doping: A Strategy for Tuning N_2 Activation towards Solar-Driven Nitrogen Fixation. *J. Am. Chem. Soc.*, 2018, **140**, 9434-9443. DOI: 10.1021/jacs.8b02076.

24 Y. Bai, L. Q. Ye, T. Chen, L. Wang, X. Shi, X. Zhang and D. Chen, Facet-Dependent Photocatalytic N_2 Fixation of Bismuth-Rich Bi_5O_7I Nanosheets. *ACS Appl. Mater. Interfaces*, 2016, **8**, 27661-27668. DOI: 10.1021/acsami.6b08129.

25 W. R. Zhao, H. P. Xi, M. Zhang, Y. J. Li, J. S. Chen, J. Zhang and X. Zhu, Enhanced quantum yield of nitrogen fixation for hydrogen storage with in situ-formed carbonaceous radicals. *Chem. Commun.,* 2015, **51**, 4785-4788. DOI: 10.1039/c5cc00589b.

26 C. L. Xiao, H. Hu, X. Y. Zhang and D. R. MacFarlane, Nanostructured Gold/Bismutite Hybrid Heterocatalysts for Plasmon-Enhanced Photosynthesis of Ammonia. *ACS Sustainable Chem. Eng.*, 2017, **5**, 10858-10863. DOI: 10.1021/acssuschemeng.7b02788.

27 Y. H. Lu, Y. Yang, T. F. Zhang, Z. Ge, H. C. Chang, P. S. Xiao, Y. Y. Xie, L. Hua, Q. Y. Li, H. Y. Li, B. Ma, N. J. Guan, Y. F. Ma and Y. S. Chen, Photoprompted Hot Electrons from Bulk Cross-Linked Graphene Materials and Their Efficient Catalysis for Atmospheric Ammonia Synthesis. *ACS Nano*, 2016, **10**, 10507-10515. DOI: 10.1021/acsnano.6b06472.

28 A. Banerjee, B. D. Yuhas, E. A. Margulies, Y. B. Zhang, Y. Shim, M. R. Wasielewski and M. G. Kanatzidis, Photochemical Nitrogen Conversion to Ammonia in Ambient Conditions with FeMoS-Chalcogels. *J. Am. Chem. Soc.*, 2015, **137**, 2030-2034. DOI: 10.1021/ja512491v.

29 J. Liu, M. S. Kelley, W. Q. Wu, A. Banerjee, A. P. Douvalisc, J. S. Wu, Y. B. Zhang, G. C. Schatz and M. G. Kanatzidis, Nitrogenase-mimic iron-containing chalcogels for photochemical reduction of dinitrogen to ammonia. *PNAS*, 2016, **113**, 5530-5535. DOI: org/10.1073/pnas.1605512113.